Article

Borate–pyran lean electrolyte-based Li-metal batteries with minimal Li corrosion

Hyeokjin Kwon [1], Hongsin Kim[2], Jaemin Hwang [1], Wonsik Oh [1], Youngil Roh[1], Dongseok Shin[2] & Hee-Tak Kim [1,3] ✉

Engineering liquid electrolytes for lithium (Li)-metal electrodes has been used to control the morphology of deposited Li in Li-metal batteries (LMBs). However, the Li corrosion problem remains unresolved, hindering the design of lean electrolytes for practical LMBs, which require the electrolyte/capacity (E/C) ratio to be 2 g Ah^{-1} or lower. Here we report a borate–pyran-based electrolyte to address the chronic Li-corrosion problem. We discovered that the borate–pyran electrolyte transforms large LiF crystallites in the solid–electrolyte interphase into fine crystalline or glassy LiF, which enhances the passivity of the Li/electrolyte interface by minimizing the permeation of electrolyte molecules into the solid–electrolyte interphase. LMBs assembled with the borate–pyran electrolyte, a high-nickel layered oxide cathode (3.83 mAh cm^{-2}) and thin lithium (20 μm) delivered a high initial full-cell-level energy density (>400 Wh kg^{-1}) and operated for 400 cycles with 70% capacity retention at an E/C ratio of 1.92 g Ah^{-1}, 350 cycles with 73% capacity retention at 1.24 g Ah^{-1} and 200 cycles with 85% retention at 0.96 g Ah^{-1}.

Lithium (Li) metal is the most targeted anode material for rechargeable batteries[1]. However, repeated Li plating/stripping result in the evolution of a ramified or rough structure with an expanded electroactive surface. The roughening of the electrode accompanies the repeated collapse and regeneration of a solid–electrolyte interphase (SEI), exhausting the liquid electrolyte and Li, leaving an inactive Li layer on the Li-metal electrode surface[2,3] and eventually leading to cell failure[4].

Liquid electrolyte engineering for Li-metal anodes has aimed to generate the SEI forming flat and compact Li deposits and thus improving the reversibility of the Li anode. In particular, recently reported high-concentration electrolytes (HCEs)[5,6], local high-concentration electrolytes (LHCEs)[7,8] and electrolytes with fluorinated solvents[9,10] have been designed to form SEIs in which desired components (for example, LiF, Li$_2$O, Li$_2$S and LiN$_x$O$_y$ crystallites or organic materials with good physicochemical properties[11,12]) are uniformly distributed via the preferential decomposition of certain electrolyte species (for example, LiFSI or fluorinated solvents).

Although the electrolytes can extend the lifespan of Li-metal batteries (LMBs) by regulating the morphology of deposited Li, the constant consumption of the electrolyte by reaction with Li (referred to as Li corrosion) hinders further progress[3]. As reported by Cui and co-workers[13], the recently developed electrolytes show similar or worse corrosion properties compared to conventional electrolytes. Although recent strategies have partially resolved the morphological instability of Li, they struggle to minimize Li corrosion. In particular, the large gap in the electrolyte to capacity (E/C) ratio between LMBs (>2 g Ah^{-1})[14–16] and Li-ion batteries (~1.3 g Ah^{-1})[2] reveals that an excessive amount of electrolyte is used to compensate for the electrolyte consumption of the LMBs, which reduces the advantage of their high potential energy density. In this context, depositing dense Li with minimal Li corrosion is considered a critical challenge (Fig. 1a).

Here we report a borate–pyran-based electrolyte that can address the chronic Li corrosion problem. This electrolyte enables a LMB with a high initial full cell-level energy density (>400 Wh kg^{-1}) to operate for 400 cycles with 70% capacity retention at an E/C ratio of 1.92 g Ah^{-1}, 350 cycles with 73% capacity retention at 1.24 g Ah^{-1} and 200 cycles with 85% retention at 0.96 g Ah^{-1}, which exceeds the performances of state-of-the-art lean electrolyte LMBs[2,9,17]. The key feature of the

[1]Department of Chemical and Biomolecular Engineering, KAIST, Daejeon, Republic of Korea. [2]Battery R&D, LG Energy Solution, Daejeon, Republic of Korea. [3]LG Energy Solution-KAIST Frontier Research Lab, KAIST, Daejeon, Republic of Korea. ✉e-mail: heetak.kim@kaist.ac.kr
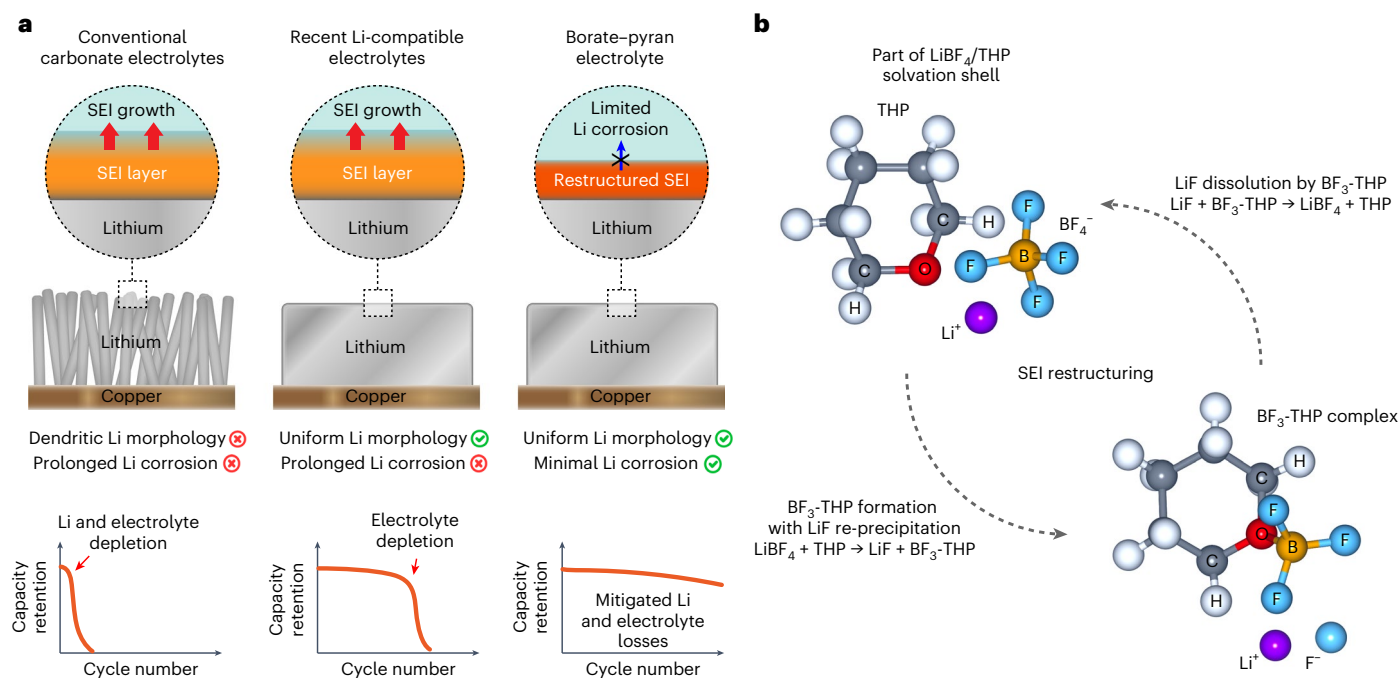
Fig. 1 | Electrolyte design principles for lean electrolyte LMBs with minimal Li corrosion. a, A scheme of electrolyte design strategy of the borate–pyran electrolyte. The conventional carbonate electrolyte exhibits dendritic Li morphology and Li corrosiveness, leading to the depletion of both Li and the electrolyte with a rapid drop in cell capacity. Recently developed LHCE exhibit a uniform Li morphology but still suffer from electrolyte depletion due to persistent Li corrosiveness showing sudden capacity drop. In contrast, the borate–pyran electrolyte not only maintains a uniform Li morphology but also limits Li corrosion by a restructured SEI, mitigating the depletion of Li and the electrolyte and enabling extended cycle life. **b**, A chemical process of SEI restructuring in the borate–pyran electrolyte. The reaction of BF_3-THP formation from THP and BF_4^- and its reverse reaction (that is, dissolution of LiF by the BF_3-THP) restructures LiF-containing SEI on Li with the borate–pyran electrolyte.

electrolyte presented in this work is that it restructures large LiF crystallites that are initially formed in the SEI into fine crystalline or glassy LiF to minimize Li corrosion in contrast with the prolonged Li corrosion occurring in conventional electrolytes (Fig. 1a). The minimized Li corrosion via LiF restructuring reduces Li and electrolyte losses, enabling the development of lean electrolyte LMBs. We propose a mechanism for LiF restructuring that involves the boron trifluoride–pyran adduct-mediated dissolution and re-precipitation of LiF in the SEI (Fig. 1b).

Interphase restructuring in borate–pyran electrolyte

The SEI structure is determined by the accumulation of insoluble by-products of Li corrosion[13,18,19]. We used cryogenic transmission electron microscopy (cryo-TEM), fast-Fourier transform (FFT) and inverse FFT imaging to investigate the structural evolution of the SEI on the Li-metal surface for a conventional carbonate and ether electrolyte after Li plating and subsequent ageing for 12 h. As shown in Fig. 2a,b, a carbonate electrolyte (1 M lithium hexafluorophosphate (LiPF$_6$) in ethylene carbonate (EC):ethyl methyl carbonate (EMC) + 2 wt% vinylene carbonate (VC), denoted as LiPF$_6$ EC:EMC:VC) formed a mosaic-structured SEI containing LiF, Li$_2$O and carbonate species, consistent with the X-ray photoelectron spectroscopy (XPS) profiles (Supplementary Fig. 1) and previous observations of the SEI formed in carbonate solvents[3,20]. The carbonate electrolyte showed a 44.1% increase in SEI thickness during ageing (Fig. 2c). A recently developed LHCE (lithium bis(fluorosulfonyl)imide (LiFSI) in 1,2-dimethoxyethane (DME):1,1,2,2-tetrafluoroethyl-2,2,3,3-tetrafluoropropyl ether (TTE), denoted as LiFSI DME:TTE) formed an amorphous SEI structure (Fig. 2a,b) with LiFSI-driven SEI components (LiF or sulfur species; Supplementary Fig. 2), which was similar to the LiFSI and fluorinated

solvent-based electrolytes[9,10,21]. The LHCE showed an 88.1% increase in SEI layer thickness during 12 h of Li passivation (Fig. 2c), indicating a faster SEI growth than the carbonate electrolyte. In accordance with previous observations[13], Li corrosion caused an increase in SEI thickness for the carbonate and LHCE electrolytes, while the nanoscale SEI fine structure hardly changed during the SEI evolution.

We propose an electrolyte, consisting of four components, that can minimize Li corrosion: lithium tetrafluoroborate (LiBF$_4$) and tetrahydropyran (THP) (which induce LiF restructuring, as described later), lithium bis(trifluoromethanesulfonyl)imide (LiTFSI) (which imparts ionic conductivity to the LiBF$_4$ THP electrolyte) and fluoroethylene carbonate (FEC) (which forms an initial LiF-enriched SEI to be restructured by LiBF$_4$ THP). The composition of the electrolyte (hereafter referred to as borate–pyran electrolyte) was 0.4 M LiBF$_4$, 0.4 M LiTFSI THP + 20% FEC. The SEI formed on as-deposited Li in the borate–pyran electrolyte contained LiF crystallites, as indicated by the LiF(111) and LiF(220) signals in the FFT images (Fig. 2a) and the LiF content in the XPS spectra (Fig. 2d and Supplementary Fig. 3). The LiF crystallites were scattered across the SEI, as highlighted by the inverse FFT image in Fig. 2b. Surprisingly, during Li passivation, the large LiF crystallites were transformed into uniformly distributed fine LiF crystallites (termed 'LiF restructuring'). The intense spot signals originating from the large LiF crystallites in the FFT images changed to smooth ring patterns after ageing. The structural transformation was not accompanied by notable changes in the atomic concentration or chemical structure of the SEI layer, as indicated by the XPS survey scan, O 1s and F 1s spectra before (Fig. 2d) and after (Fig. 2e) ageing; this rules out the irreversible dissolution of LiF crystallites. The SEI thickness showed only a slight decrease (4.1%) during 12 h of storage (Fig. 2c and Supplementary Fig. 4), in contrast with the carbonate (44.1% increase) and LHCE (88.1% increase) electrolytes.
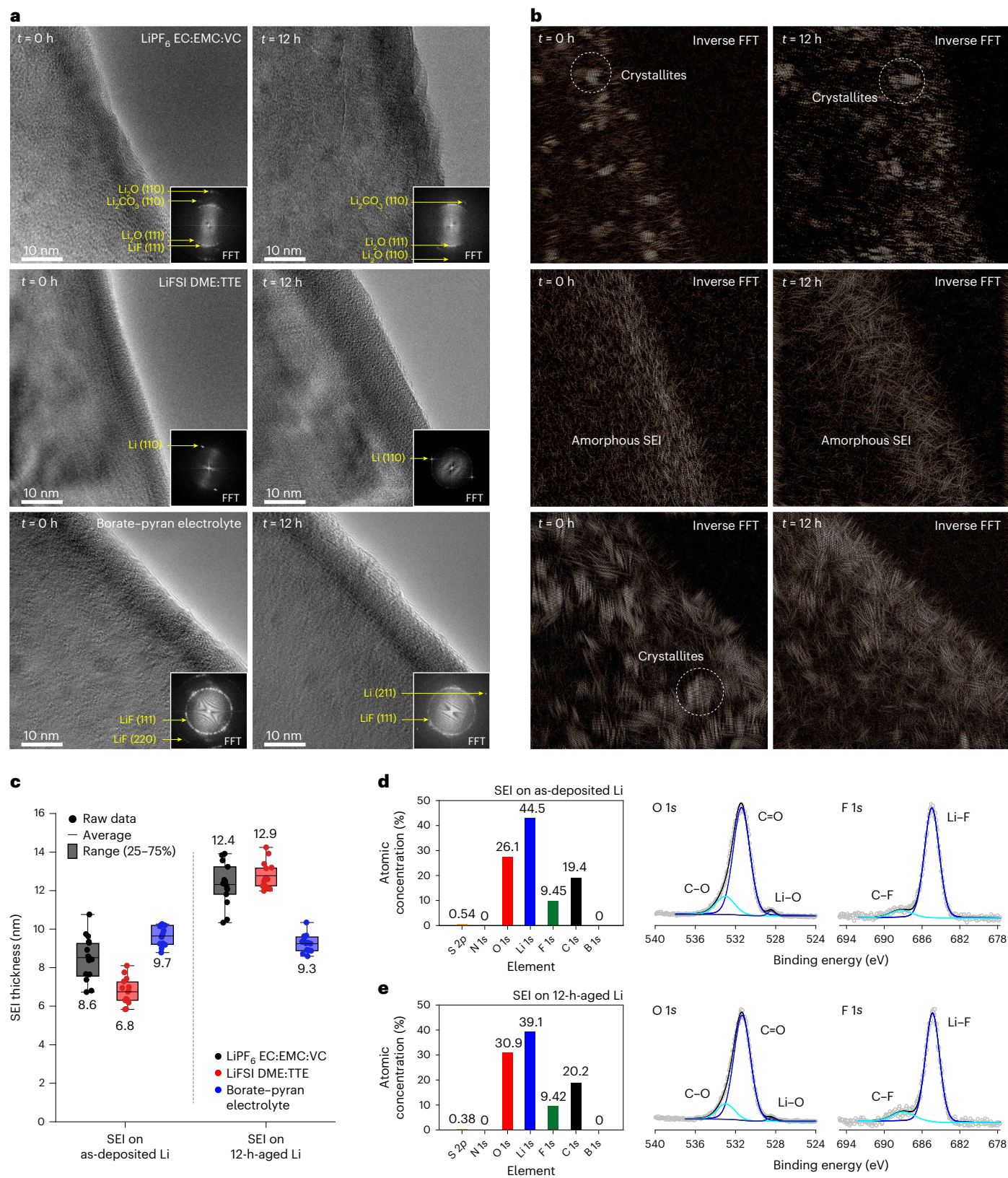
Fig. 2 | Investigation of structural changes in SEI upon ageing. a,b, Cryo-TEM (**a**), corresponding FFT (insets) and inverse FFT (**b**) images obtained from crystallite signals of SEI layers formed on Li-metal deposit (1.0 mA cm^{-2}, 1.0 mAh cm^{-2}) in LiPF$_6$ EC:EMC:VC, LiFSI DME:TTE and borate–pyran electrolytes at $t = 0$ and 12 h (t represents the storage time after completion of Li deposition). **c,** Thickness of SEI on as-deposited Li and 12-h-aged Li. The data are represented by measuring the thickness of different locations ($n = 14$) for each sample. Dots represent raw data, boxes represent the 25–75% range, and in-box horizontal lines represent mean values. The whisker lines represent the maximum and minimum values without outliers. **d,e,** Atomic concentrations obtained from XPS survey scan and deconvoluted O 1s and F 1s XPS spectra of SEI for the borate–pyran electrolyte before (**d**) and after (**e**) 12 h ageing.
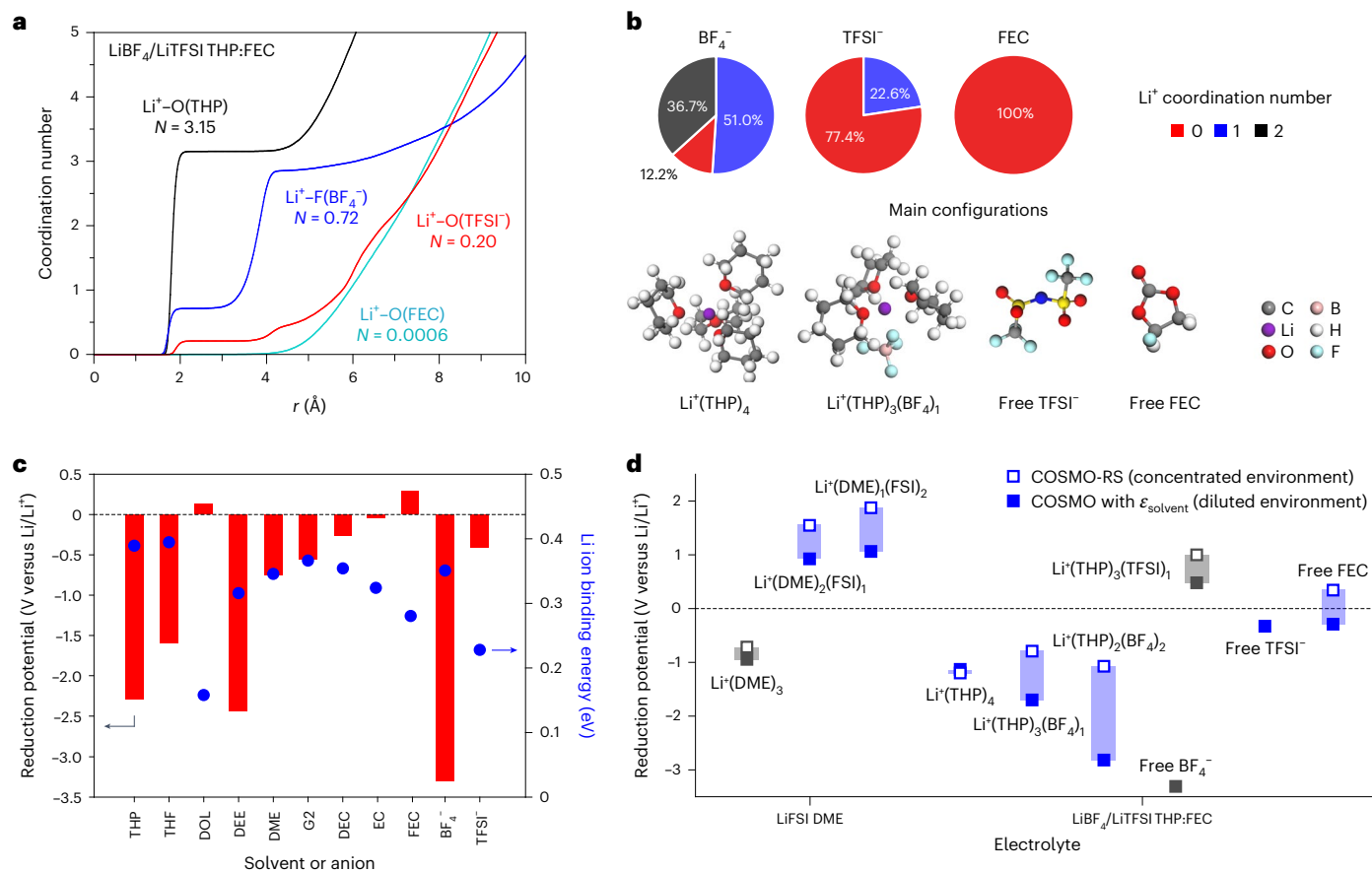
Fig. 3 | Solvation structure and reduction stability. a, Coordination number (N) obtained from radial distribution functions calculated by MD simulations. r, radial distance from Li$^+$. **b**, Coordination number distributions within LiBF$_4$, LiTFSI and FEC in the borate–pyran electrolyte, along with snapshots of the dominant structures for the electrolyte. **c**, Reduction potentials and Li$^+$ binding energies of various organic solvents and anions (THP, tetrahydrofuran (THF), 1,3-dioxolane (DOL), diethyl ether (DEE), DME, diglyme (G2), diethyl carbonate (DEC), EC, FEC, BF$_4^-$ and TFSI$^-$). **d**, Comparison of reduction potentials of solvent and salt configurations of a typical ether electrolyte (LiFSI DME) and borate–pyran electrolyte (LiBF$_4$/LiTFSI THP:FEC). Taking into account that the reduction potential varies with concentration, the reduction potentials for concentrated (COSMO-RS model) and diluted (COSMO with $\varepsilon_{solvent}$) environments are calculated separately and presented as a range. The grey symbols represent a molecule/Li$^+$ solvate with a population of less than 1%.

FEC-free LiBF$_4$/LiTFSI THP electrolyte showed low LiF and high B–F signal intensities in the XPS spectra, while FEC-containing electrolytes (0.4 M LiTFSI THP:FEC, 0.4 M LiBF$_4$ THP:FEC and 0.4 M LiTFSI/0.4 M LiBF$_4$ THP:FEC) exhibited weak boron and strong LiF signals (Supplementary Fig. 5) and similar LiF crystallite size (~7 nm; Supplementary Fig. 6). These results suggest that the initial SEI layer formation can be attributed to the decomposition of the FEC. Meanwhile, storing the deposited Li in the LiBF$_4$-free electrolyte did not lead to restructuring of LiF (Supplementary Figs. 7 and 8); this observation indicates that the restructuring of the preformed LiF can be ascribed to a chemical process of LiBF$_4$.

Reduction stability of borate–pyran electrolyte

The successful regulation of Li corrosion in liquid electrolytes requires not only a finely passivated interphase but also a high reduction stability of electrolyte molecules and Li$^+$ solvates in the liquid electrolyte[18,22–24]. The reduction stabilities were assessed by calculating solvation structure of electrolytes and corresponding reduction potential via density functional theory (DFT) and molecular dynamics (MD) simulations.

In the borate–pyran electrolyte, the THP was mainly involved in the primary Li$^+$ solvation shell (coordination number of 3.2), while the other components showed a relatively low participation in the primary shell (coordination numbers of 0.20 for TFSI$^-$, 0.72 for BF$_4^-$ and 0.0006 for FEC; Fig. 3a and Supplementary Fig. 9). An 87.7% fraction of BF$_4^-$ participated in Li$^+$ solvation, whereas 77.4% of TFSI$^-$ existed in free state

(Fig. 3b and Supplementary Fig. 10a–d). FEC molecules almost exist in free state due to the weak Li$^+$ binding energy associated with the electron-withdrawing fluorine group[25]. Notably, the relative population of the TFSI$^-$ anions involved in the Li$^+$ solvation with respect to the total amount of free solvents/anions and Li$^+$ solvates in the borate–pyran electrolyte is only 0.9% (Supplementary Fig. 10e), thereby decreasing the probability of TFSI$^-$ decomposition at the Li anode. As shown in Fig. 3c, THP showed a high Li$^+$ binding energy and a low reduction potential compared to many solvent candidates, indicating that it is a well-balanced solvent fulfilling the high Li$^+$-solvating power and high reduction stability requirements. The cycling stability of LMBs under lean electrolyte condition increased with decreasing reduction potential of the solvent candidates (Supplementary Fig. 11), which supports the above argument.

The reduction potentials of the salt and solvent structures identified in the borate–pyran electrolyte were calculated using DFT simulations and are compared in Fig. 3d. To evaluate the reduction stability of the borate–pyran electrolyte, we compared it with that of a typical ether-based electrolyte, 4 M LiFSI DME. The two main THP-containing Li$^+$ solvates in the borate–pyran electrolyte, Li$^+$(THP)$_3$(BF$_4^-$)$_1$ and Li$^+$(THP)$_4$, had reduction potentials of −1.71 to −0.79 V and −1.21 to −1.14 V versus Li/Li$^+$, respectively, denoting a high stability against reductive decomposition. The inclusion of BF$_4^-$ in the Li$^+$ solvation shell did not negatively affect the reduction stability, as indicated by the low reduction potentials of the BF$_4^-$-containing Li$^+$ solvates. For the
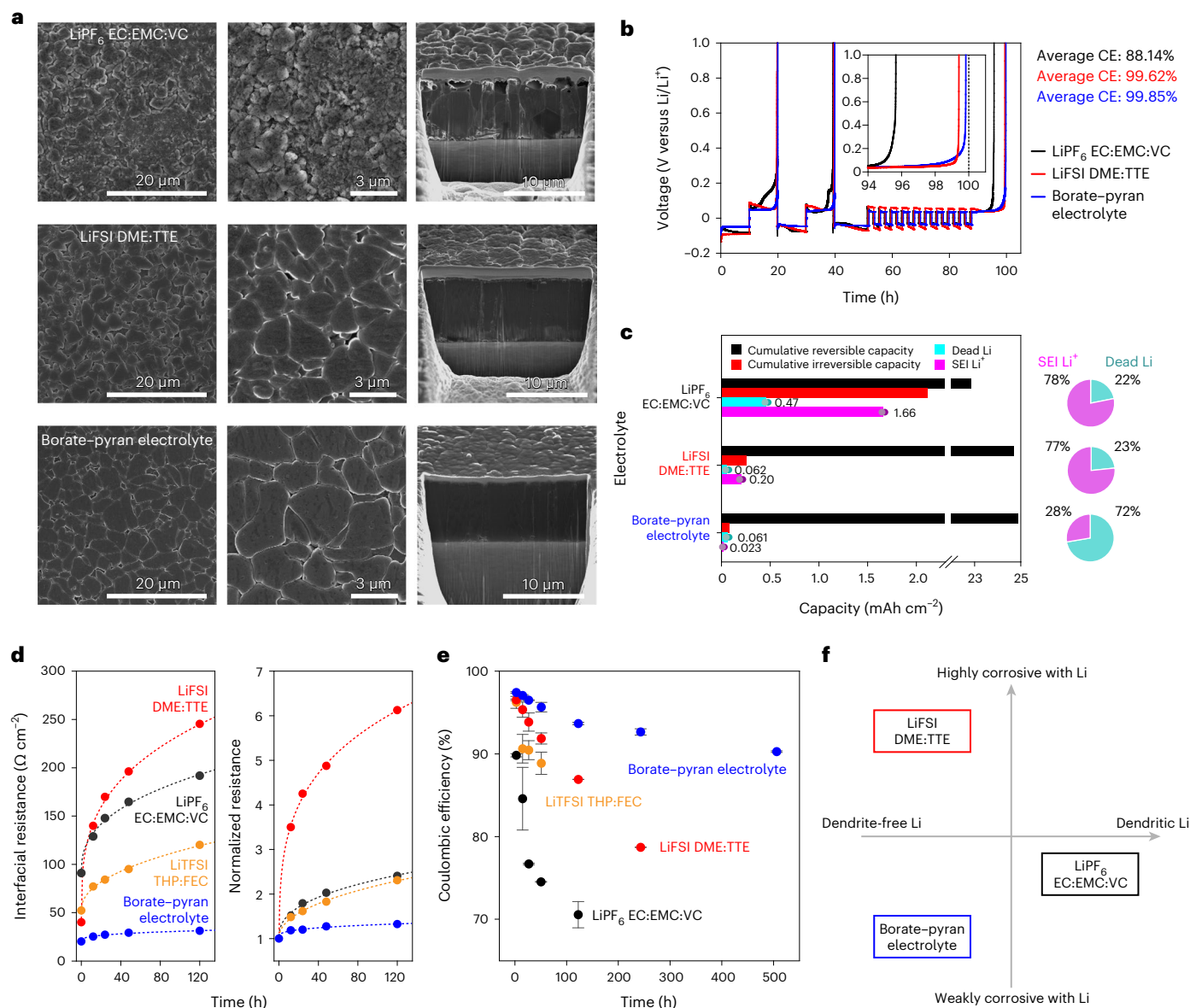
Fig. 4 | Reversibility and corrosivity of Li-metal electrode in liquid electrolytes. a, SEM images showing the top view (left, middle) and cross-section (right) morphology of Li deposits (2 mAh cm^{-2}) plated on Cu current collector under 290 kPa pressure at 0.5 mA cm^{-2}. **b**, Measurement of CE of Li plating/stripping in Li||Cu cells using a modified Aurbach method. Inset: measurement of CE from 94 h to 101 h. **c**, Cumulative reversible capacity, cumulative irreversible capacity and irreversible capacities from SEI and dead Li formation. For data visibility, an *x*-axis break in the range of 2.3–22 mAh cm^{-2} was applied. The pie charts on the right show the fractions of loss due to SEI or dead Li formation. Each

dot indicates two replicated TGC quantification (*n* = 2) with the same electrolyte. **d**, Time-dependent changes of interfacial resistance in Li||Li coin cells and of normalized interfacial resistance with respect to initial resistance (*t* = 0). The fitting curves represent nonlinear least squares fit to a power law ($R_{interface} \propto at^x$) (ref. 13). **e**, Storage time dependence of CE of Li plating/ageing/stripping in Li||Cu coin cells. The whiskers represent the range between a pair of measurements (*n* = 2), and the dots are the means. **f**, Quadrant chart comparing uniformity of Li morphology and Li corrosivity for different electrolytes.

LiFSI DME electrolyte, the main Li$^+$ solvation shells, Li$^+$(DME)$_1$(FSI$^-$)$_2$ and Li$^+$(DME)$_2$(FSI$^-$)$_1$ (Supplementary Figs. 12 and 13), had high reduction potentials of 1.07–1.89 V and 0.93–1.57 V versus Li/Li$^+$, respectively, in agreement with previous studies[10,26]. The high reduction stability of the THP-containing Li$^+$ solvates was experimentally verified by the reduced cathodic currents observed for the borate–pyran electrolyte in a linear sweep voltammetry test (Supplementary Fig. 14).

TFSI$^-$ had reduction potentials of 0.48–1.01 V and −0.33 V versus Li/Li$^+$ in the Li$^+$-coordinated and free molecular states, respectively, showing that the decoordination of TFSI$^-$ by THP enhances the reduction stability of TFSI$^-$. The calculated reduction potential of free FEC was −0.29 to 0.35 V versus Li/Li$^+$. The much higher atomic content of

fluorine (~10 at%) than nitrogen, sulfur or boron species (<1 at%) in the SEI with the borate–pyran electrolyte (Fig. 2c and Supplementary Fig. 3) demonstrates the predominant participation of FEC and the weak involvement of TFSI$^-$ and BF$_4^-$ in the initial SEI formation. LiTFSI is highly dissociated in the electrolyte, resulting in a high ionic conductivity (Supplementary Figs. 15–17 and Supplementary Note 1).

Suppressed Li corrosion in borate–pyran electrolyte

As shown by the scanning electron microscopy (SEM) images of the Li deposits under pressure (Fig. 4a and Supplementary Figs. 18 and 19), the carbonate electrolyte resulted in a mossy morphology; in
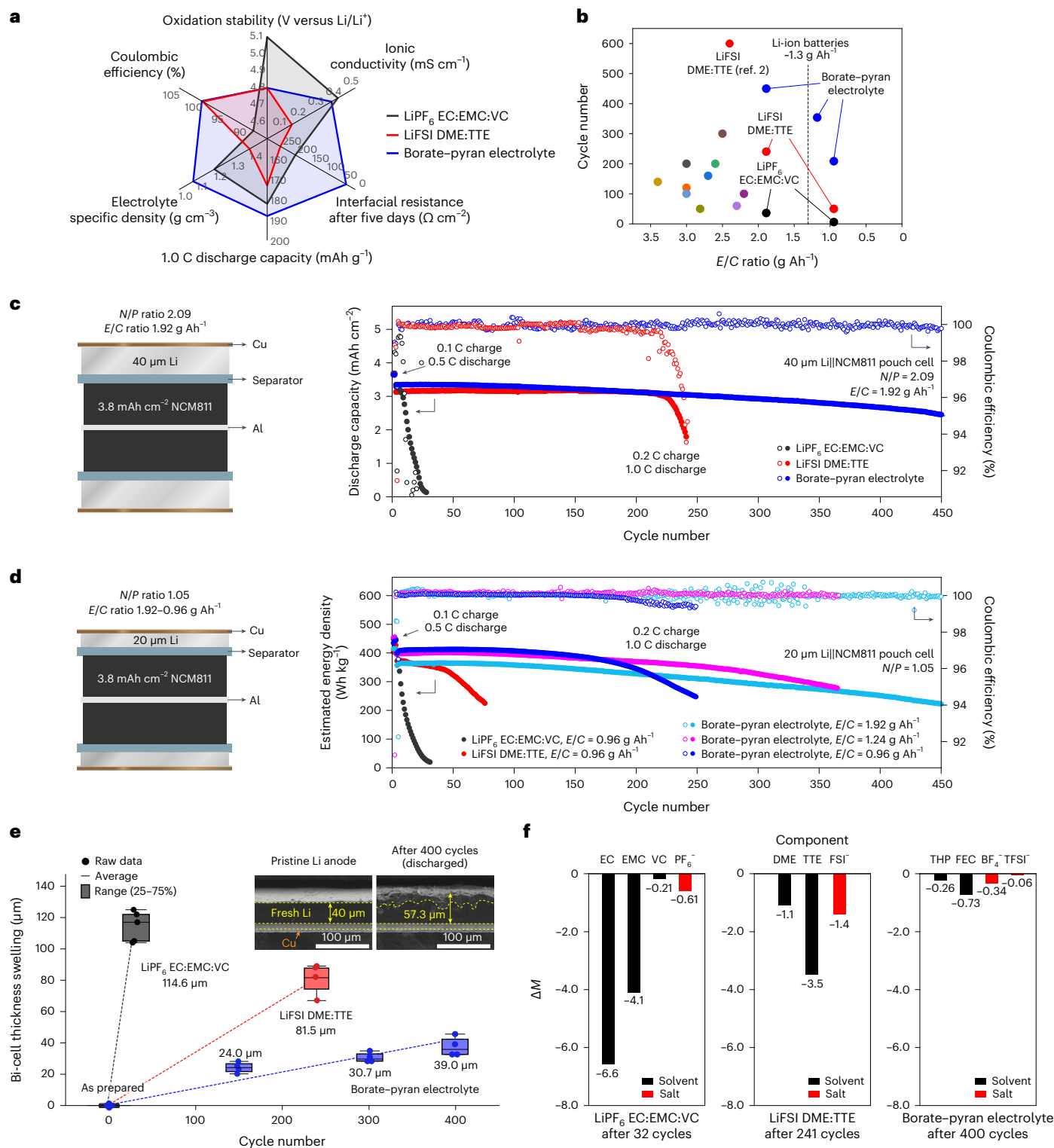
Fig. 5 | Pouch cell performance and post-mortem analyses. a, Radar plot of physical and electrochemical properties of electrolytes. **b,** E/C ratios and cycle numbers of previously reported state-of-the-art LMB pouch cells and prototype pouch cells presented in this work. **c,** Configuration of 40 μm Li||NCM811 bi-cell, and the cycle performances of 40 μm Li||NCM811 pouch cells with LiPF$_6$ EC:EMC:VC, LiFSI DME:TTE and borate–pyran electrolyte at E/C ratio of 1.92 g Ah^{-1}. N/P is a negative to positive areal capacity ratio. **d,** Configuration of 20 μm Li||NCM811 bi-cell and the cycle performances of 20 μm Li||NCM811 pouch cells with LiPF$_6$ EC:EMC:VC, LiFSI DME:TTE (0.96 g Ah^{-1}) and borate–pyran electrolyte at various E/C ratios (1.92, 1.24 and 0.96 g Ah^{-1}). **e,** Cycle number

dependence of thickness of 40 μm Li||NCM811 bi-cells for the carbonate, LHCE and borate–pyran electrolytes. The data are statistically represented by measuring the thickness of different locations ($n = 4$) for each pouch cell. Dots represent raw data, boxes represent the 25–75% range, in-box horizontal lines represent mean values and numbers indicate the change in bi-cell thickness. The whisker lines represent the maximum and minimum values without outliers. The trend line representing cell swelling ratio is provided as a dash line. Inset: cross-section SEM images of pristine Li and Li anode after 400 cycles in the borate–pyran electrolyte. **f,** Amount of electrolyte components consumed during cycling quantified by NMR.
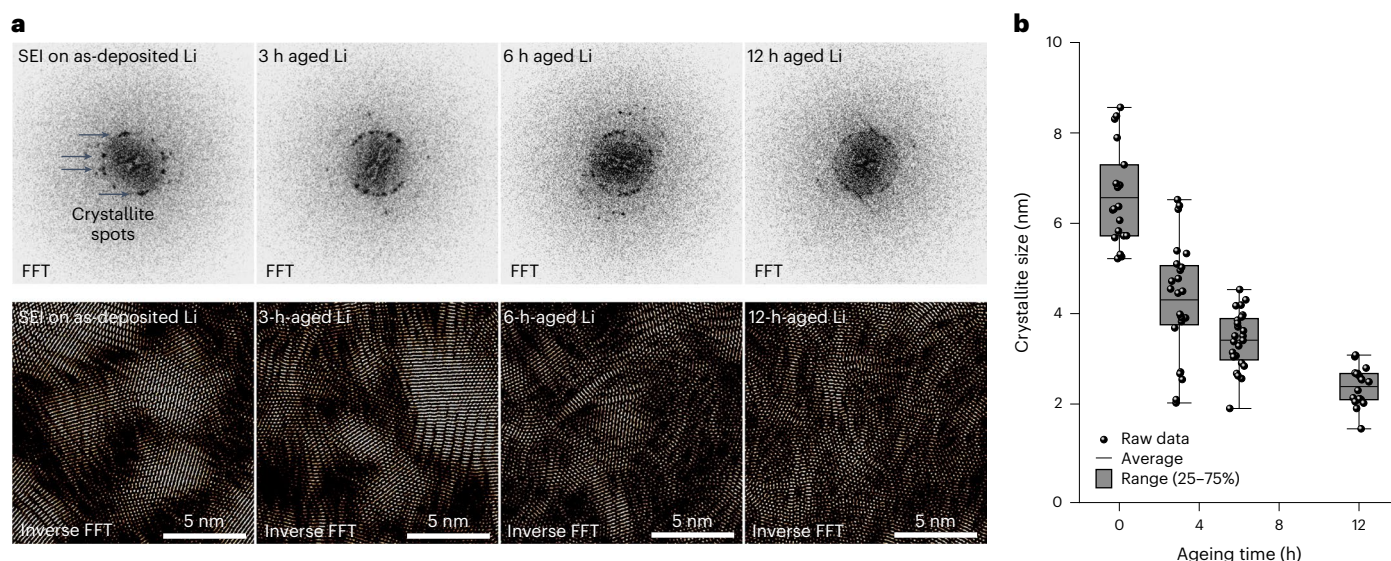
Fig. 6 | Investigation of LiF fine structure. a,b, FFT images and inverse FFT images for LiF in the SEI layer formed on as-deposited and aged Li in the borate–pyran electrolyte (**a**) and size distribution of crystalline LiF (**b**). The size distribution of crystalline LiF is statistically shown by measuring the diameter of the circle of equal perimeter of each crystallite ($n = 19$) over ageing time. Dots represent raw data, boxes represent the 25–75% range and in-box horizontal lines represent mean values. The whisker lines represent the maximum and minimum values without outliers.

contrast, the LHCE and borate–pyran electrolytes led to a dendrite-free Li surface morphology with a grain size of about 3 μm, along with a densely packed cross-sectional morphology. The LiBF$_4$-free LiTFSI THP:FEC electrolyte did not produce such uniform morphology (Supplementary Fig. 19c).

We measured the Coulombic efficiency (CE) of Li plating/stripping on a deposited Li using the modified Aurbach method[27]. As shown in Fig. 4b, after the first two cycles (measured CEs of the first two cycles were provided in Supplementary Fig. 20), the average efficiencies of Li plating/stripping in the carbonate and LHCE electrolytes were 88.14% and 99.62%, respectively. The value obtained for the LHCE electrolyte is similar to those of recently reported LHCEs[21] or fluorinated solvent electrolytes[9,10]. Apart from being among the best-performing reported electrolytes, the borate–pyran electrolyte exhibited an average efficiency (99.85%) higher than that measured for the LHCE. Li||Cu cell also showed stable cycling of Li plating/stripping in the borate–pyran electrolyte (Supplementary Fig. 21).

The Li losses from dead Li and SEI formation during the application of the Aurbach protocol were distinguished using titration gas chromatography[3,28] (TGC; Supplementary Fig. 22). As shown in Fig. 4c, for the carbonate, LHCE and borate–pyran electrolytes, 1.86% (0.47 mAh cm^{-2}), 0.25% (0.062 mAh cm^{-2}) and 0.24% (0.061 mAh cm^{-2}) of the total capacities were spent in the formation of dead Li, respectively, and 6.65% (1.66 mAh cm^{-2}), 0.82% (0.20 mAh cm^{-2}) and 0.093% (0.023 mAh cm^{-2}) of the total capacities were consumed by SEI formation, respectively. The fractions of SEI formation to total Li loss for the carbonate and LHCE electrolytes were 78% and 77%, respectively, while 28% for the borate–pyran electrolyte, further confirming its low corrosivity.

The Li corrosivity of the electrolytes was further assessed by examining the time-dependent changes of the interfacial resistance ($R_\text{interface}$; Fig. 4d), which typically corresponds to the resistance of SEI[13,29,30]. The carbonate electrolyte showed an initial $R_\text{interface}$ of 90 Ω cm^{-2} and 2.5-fold increase during ageing for five days. Despite the smaller initial $R_\text{interface}$, the LHCE exhibited a larger $R_\text{interface}$ increase (6-fold) during ageing for 5 days than the carbonate electrolyte because of the highly corrosive nature of LiFSI. Among the studied electrolytes, the borate–pyran electrolyte exhibited the lowest initial $R_\text{interface}$ value (20 Ω cm^{-2}) and smallest increase in $R_\text{interface}$ upon ageing (1.5-fold during ageing for 5 days). The time-dependent changes in $R_\text{interface}$ for various electrolyte

formulations show that the combination of LiBF$_4$ and THP:FEC leads to stable $R_\text{interface}$ values (Supplementary Fig. 23).

The corrosivity of deposited Li in different electrolytes was quantified by measuring the CE at varying ageing times[13] as shown in Fig. 4e. Extending the ageing time from 5 min to 2 days resulted in a decrease in CE by 10.70% for the carbonate electrolyte and by 4.70% for the LHCE, in contrast with the decrease of only 1.02% for the borate–pyran electrolyte. Even after 21 days of storage, the CE in the borate–pyran electrolyte remained higher than 90%. The removal of LiBF$_4$ from the electrolyte (that is, LiTFSI THP:FEC) resulted in a CE drop below 90% after 2 days of storage. The average corrosion rates for the carbonate, LHCE and borate–pyran electrolytes were approximately 0.87, 0.83 and 0.15 μAh cm^{-2} h^{-1} after 48 h, respectively (Supplementary Fig. 24). The corrosion rate for the borate–pyran electrolyte was comparable to that of lithiated Si anodes[31,32] and slightly higher than that of lithiated graphite anodes[33]. On the basis of the results in this section, the borate–pyran electrolyte can be located in the weak Li corrosiveness/uniform Li morphology sector of the corresponding quadrant plot shown in Fig. 4f, which is regarded as ideal to minimize the irreversibility of Li plating/stripping[13].

Lean electrolyte Li||NCM811 pouch cell performance

Physical and electrochemical properties were compared for the electrolytes (Fig. 5a). The borate–pyran electrolyte is compatible with 4 V class cathodes, as indicated by its oxidation stability up to 4.8 V versus Li/Li$^+$ in Li||Al cells (Supplementary Figs. 25 and 26). Because of its comparable ionic conductivity (0.35 mS cm^{-1} with a separator; Supplementary Fig. 27) and small $R_\text{interface}$ (31 Ω cm^{-2} after five days; Fig. 3d), the borate–pyran electrolyte showed a higher rate capability than the other two electrolytes (Supplementary Fig. 28). Moreover, the borate–pyran electrolyte has low specific density (1.1 g ml^{-1}) and high Li plating/stripping reversibility (Fig. 3b), which are the key requirements for high-performance lean electrolyte LMBs.

We fabricated and tested pouch-type full cells consisting of double side-coated NCM811 (3.83 mAh cm^{-2} per side) and two Li anode pieces (40 μm or 20 μm, N/P ratio = 2.09 or 1.05, respectively) with low E/C ratios (1.92, 1.24 and 0.96 g Ah^{-1}) (Fig. 5b). The E/C ratio of 1.92 g Ah^{-1} is lower than that of state-of-the-art LMBs reported to date

(Supplementary Table 1). The E/C ratio of 0.96 g Ah^{-1} is close to the minimum electrolyte amount required to wet the cathode and separator (Supplementary Fig. 29) and comparable to that of typical LIBs. The prepared pouch cells were cycled under 286 kPa pressure (Supplementary Fig. 30).

We performed a cycling stability test on 40 µm Li||NCM811 pouch cell (E/C of 1.92 g Ah^{-1}) as shown in Fig. 5c; the carbonate electrolyte exhibited a rapid capacity drop before 20 cycles, while the pouch cell with the LHCE showed it at 220 cycles. Under the same condition, the Li||NCM811 cell with the borate–pyran electrolyte demonstrated capacity retention of 74% at 450 cycles. We further performed a cycling stability test on 20 µm Li||NCM811 pouch cells ($N/P = 1.05$). The 0.1 C discharge energy densities of the borate–pyran electrolyte correspond to 424, 458 and 474 Wh kg^{-1} at E/C values of 1.92, 1.24 and 0.96 g Ah^{-1}, respectively (Supplementary Table 2). As shown in Fig. 5d, the borate–pyran electrolyte-based cell at E/C of 1.92 g Ah^{-1} exhibited 70% energy retention after 400 cycles. The energy density delivered by the cell operating at 1.24 g Ah^{-1} and 0.96 g Ah^{-1} was higher than that of the cell operating at 1.92 g Ah^{-1} for up to 350 cycles and 200 cycles, respectively, with stable voltage profiles (Supplementary Fig. 31). By contrast, the other two electrolytes reached 70% energy retention before 50 cycles at 0.96 g Ah^{-1}. Comparing 40 µm or 20 µm thick Li anodes, the thinner Li foil exhibited higher cycling stability at 1.24 and 0.96 g Ah^{-1} (Supplementary Fig. 32), consistent with findings reported in previous work[2]. For Li||NCM523 cells and anode-free cells, the efficacy of the borate–pyran electrolyte were also demonstrated (Supplementary Figs. 33 and 34 and Supplementary Note 2).

The swelling rate of Li anode during cycling was determined from the cell thickness changes, considering nearly invariant cathode thickness during the cycling (Supplementary Fig. 35). It was 1.79 µm per cycle, 0.174 µm per cycle and 0.0488 µm per cycle for the carbonate, LHCE and borate–pyran electrolytes, respectively (Fig. 5e). For the borate–pyran electrolyte, the bi-cell thickness increased by only 39.0 µm (that is, 19.5 µm thickness increase of the single Li anode) after 400 cycles, close to that determined from the cross-sectional SEM image of the Li anode after cycling (inset of Fig. 5e, change in bi-cell thickness = 57.3 − 40.0 = 17.3 µm).

We evaluated the consumed amounts of electrolyte components in the pouch cells at 1.92 g Ah^{-1} by the nuclear magnetic resonance (NMR) spectra of the pristine and cycled electrolytes (Fig. 5f and Supplementary Figs. 36–38). The carbonate electrolyte showed a predominant consumption of the solvent components (−6.6 mol l^{-1} for EC, −4.1 mol l^{-1} for EMC) compared to the anion consumption (−0.61 mol l^{-1} for PF$_6^-$). The LHCE electrolyte exhibited preferential consumption of the fluorinated solvent (TTE, −3.5 mol l^{-1}) and FSI$^-$ anion (−1.4 mol l^{-1}) showing the almost depletion of LiFSI at the end of the cell life. A lower consumption of all electrolyte components was observed in the borate–pyran system compared with the other two electrolytes, despite the longer cycling (400 cycles). FEC was the most consumed component, consistent with the predictions of DFT and MD simulations in Fig. 3c. The small consumption of TFSI$^-$ (−0.06 mol l^{-1}) is in line with the absence of sulfur and nitrogen signals in the XPS spectra of the corresponding SEI layer (Fig. 2d and Supplementary Fig. 3).

LiF restructuring mechanism

We investigated the fine structure of LiF crystallites during the SEI restructuring process using FFT and inverse FFT images (Fig. 6a,b) obtained from the high-magnification cryo-TEM images (Supplementary Fig. 39). Immediately after the Li plating, LiF crystallites with a size of 5–8 nm were observed in the SEI. After 3 h of ageing, small LiF particles of 2–3 nm appeared in the spaces separating the large LiF crystallites, involving stacking faults and narrow necks. At 6 and 12 h, the size of the LiF crystallites was reduced to 2–3 nm and a glassy LiF region clearly appeared among them. Considering that the overall
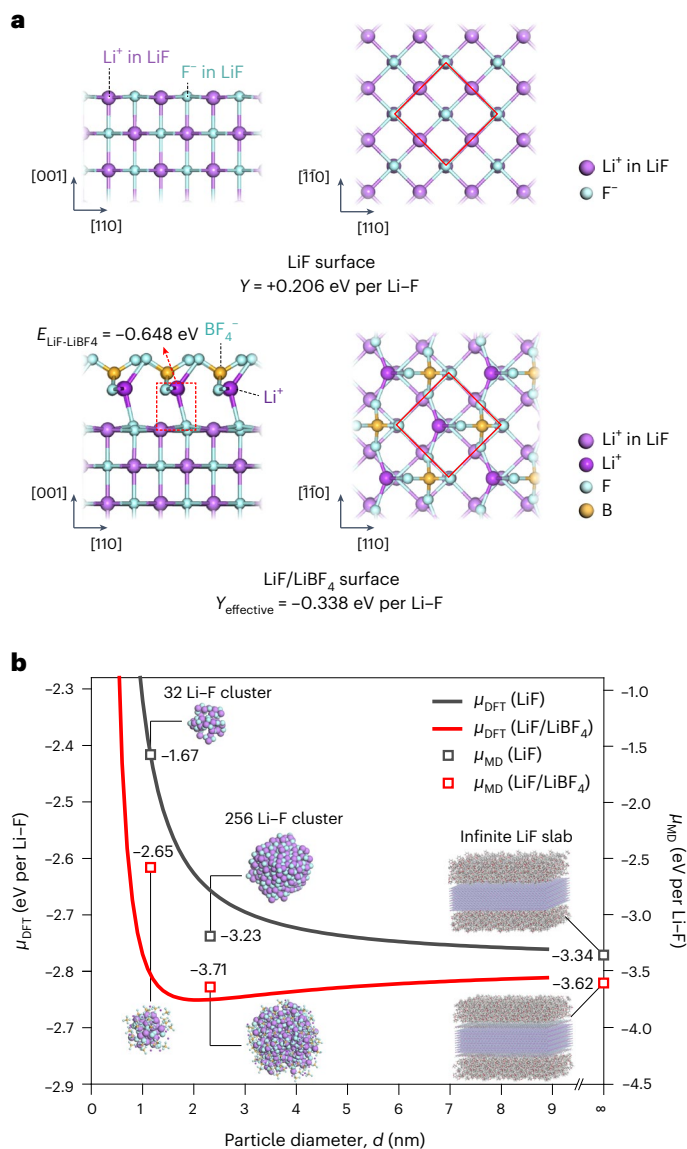
Fig. 7 | Thermodynamic feasibility of LiF restructuring. a, Atomic structures and calculated effective surface energies of clean LiF and LiBF$_4$-adsorbed surfaces (denoted as LiF/LiBF$_4$). **b**, Chemical potential (μ) of the LiF particles, along with their particle diameters, based on DFT (black or red line) or MD (black or red square symbol) simulations. An x-axis break in the range from 9 nm to infinite diameter (that is, LiF slab) was applied.

quantity of LiF remained relatively constant in the SEI (Fig. 2d,e), the cryo-TEM observation indicates that the LiF crystals in the SEI underwent a restructuring process, resulting in the formation of fine and dense structures.

Whereas the small nanoparticles are generally metastable compared to the larger ones, causing Ostwald ripening, physical or chemical interactions sufficiently strong to offset for the surface energy can result in reverse coarsening in multicomponent systems[34–39] (for example, -OH-adsorbed θ-Al$_2$O$_3$ surfaces in water[34] or oleic-acid-adsorbed Ba$_2$F$_3$Cl surfaces in alcohol[39]). The LiF restructuring requires the fulfilment of two specific criteria: (1) the formation of a small LiF particle from the initial LiF particles (~7 nm in diameter) should be thermodynamically favourable; (2) LiF can be dissolved from the initial particles and precipitated to form new particles.

To demonstrate the thermodynamic spontaneity of LiF restructuring, we performed surface energy and chemical potential calculations
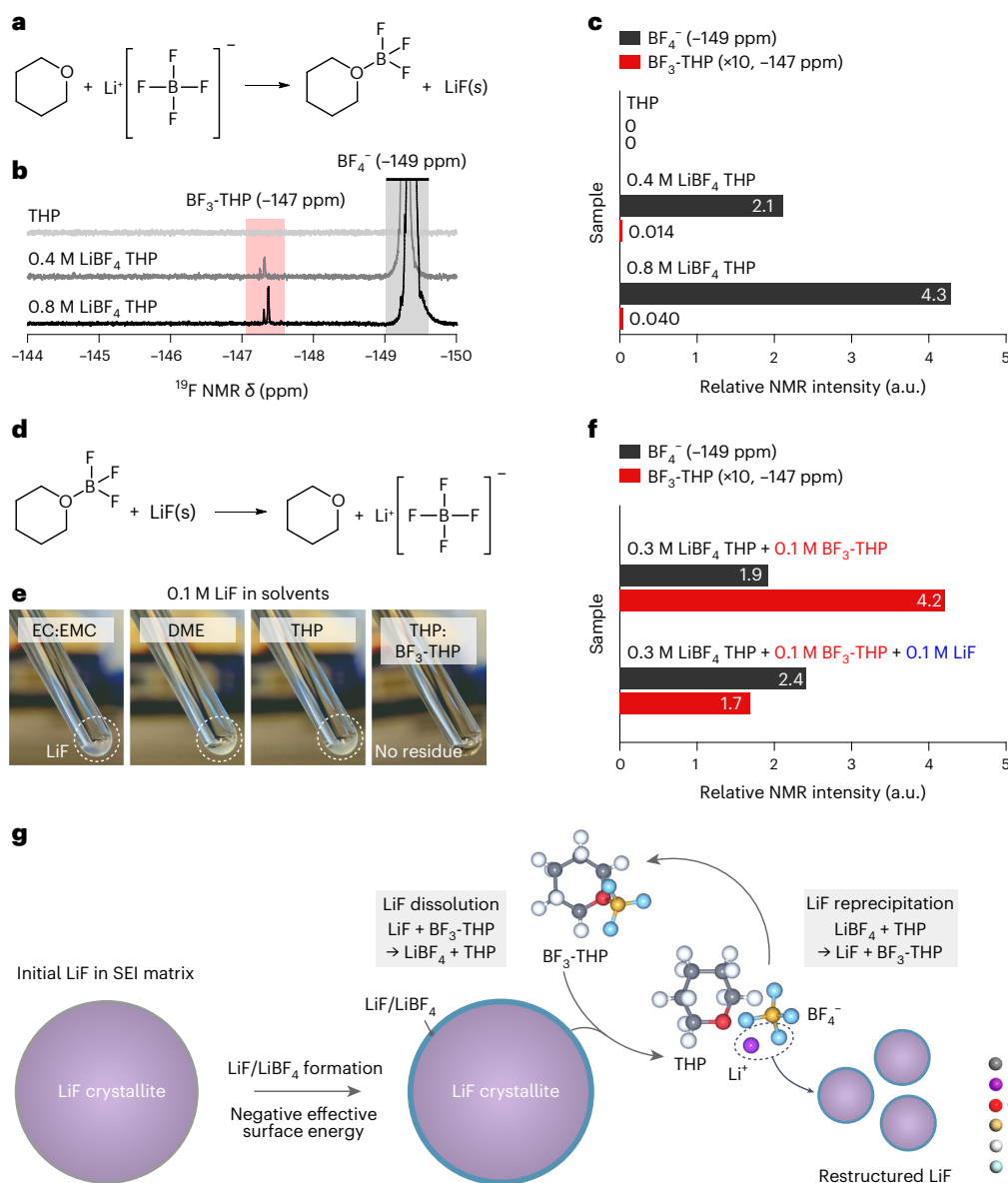
Fig. 8 | LiF restructuring mediated by BF₃-THP. a, Chemical equation of BF₃-THP formation with LiF precipitation. **b,c**, ¹⁹F NMR spectra (**b**) and the relative NMR (**c**) intensity of BF₄⁻ and BF₃-THP in THP, 0.4 M LiBF₄ THP and 0.8 M LiBF₄ THP. The same amount of fluorobenzene was added to each sample and used as a reference. **d**, Chemical equation of LiF dissolution by BF₃-THP with forming THP and LiBF₄. **e**, Digital photo of 0.1 M LiF in EC:EMC, DME, THP, and THP + 0.1 M BF₃-THP solutions. **f**, The relative NMR intensity of 0.1 M BF₃ in 0.3 M LiBF₄ THP before and after addition of 0.1 M LiF. The same amount of fluorobenzene was added to each sample and used as a reference. **g**, Schematic of the LiF restructuring mechanism that features negative effective surface energy via LiF/LiBF₄ formation and atomic diffusion of LiF mediated by BF₃-THP.

for LiF slab or particles exposed to a THP solvent environment in the presence or absence of LiBF₄ ion pairs via DFT. The surface energy of LiF slab present in the THP solvent environment is positive (+0.206 eV per Li–F; Fig. 7a and Supplementary Fig. 40a), which agrees to previous reports[40,41]. Considering the high nucleophilicity of the F site and high electrophilicity of the Li site on the LiF surface[42], we further calculated surface energy with ion pair adsorption on the LiF surface. As shown in Fig. 7a, single LiBF₄ ion pair interacts with two Li–F pairs (red square in the right top view image), resulting in a binding energy of −0.648 eV per Li–F. Compared to other salts, LiBF₄ has the largest adsorption energy and highest stability against cathodic decomposition (Supplementary Figs. 40b,c). Thus, the adsorbed LiBF₄ can effectively decrease the surface energy of LiF particles, while not being readily decomposed. The energy considering the adsorption equilibrium of LiBF₄ on LiF slab (denoted as 'LiBF₄/LiF', equation (5) in Methods) shows a negative value

of −0.338 eV per Li–F. According to our calculation, the modulated surface energy of LiF particle with LiBF₄ adsorption, which is referred to as effective surface energy, is negative when the particle size is larger than about 1 nm (Supplementary Fig. 41).

As a result of the negative effective surface energies, the chemical potential of LiBF₄-adsorbed LiF particles exhibits a local minimum at a particle diameter of 2.1 nm, in contrast to the gradually decreasing chemical potential with the particle size observed for clean LiF particles (Fig. 7b). This suggests that the large LiF particles derived from the FEC in the initial SEI structure is in a metastable state, which can be spontaneously restricted into 2 nm-size LiF particles. The prediction is in good agreement with our cryo-TEM analysis which reveals the formation of 2–3 nm LiF particles after the restructuring (Fig. 6a,b). In addition to the above DFT-based chemical potential estimates, MD-based particle formation energy calculations (square symbols in Fig. 7b) cross validate

that about ~2 nm-size LiF particles are thermodynamically more stable than larger particles.

To validate the dissolution and precipitation of LiF in the SEI matrix, we conducted an NMR analysis for LiBF$_4$ solution in THP. As shown in Fig. 8a–c, the ^{19}F NMR spectra of the 0.4 and 0.8 M LiBF$_4$ THP solutions reveal the presence of BF$_3$-THP (3.0×10^{-4} M and 6.3×10^{-4} M for 0.4 M and 0.8 M LiBF$_4$ THP), indicating the formation of the BF$_3$ adduct in the LiBF$_4$ THP solutions, according to equation (1):

$$LiBF_4\,(l) + THP\,(l) \rightarrow BF_3-THP\,(l) + LiF\,(s) \tag{1}$$
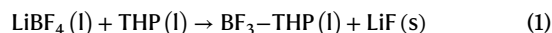
The formation of BF$_3$-THP in LiBF$_4$ THP solution is consistent with the previous literatures that ether-based solvents preferentially form stable adduct with BF$_3$[43–46], which are further confirmed by the NMR experiments and free energy calculations (Supplementary Fig. 42). The release of LiF in the bulk electrolyte phase does not influence the battery performance because of its low content (Supplementary Fig. 43 and Supplementary Note 3).

BF$_3$ or its adducts (for example, BF$_3$-ether) can react with LiF to form LiBF$_4$, resulting in LiF dissolution[47–49], which is demonstrated in Fig. 8d,e; 0.1 M LiF was soluble in THP + 0.1 M BF$_3$-THP, whereas an opaque LiF residue remained in 0.1 M LiF-containing EC:EMC, DME or THP. We observed the changes of the ^{19}F NMR signals from BF$_3$-THP (−147 ppm) and BF$_4^-$ (−149 ppm) with the addition of 0.1 M LiF salt in a solution of 0.1 M BF$_3$-THP in 0.3 M LiBF$_4$ THP (Fig. 8f). The addition of the LiF salt led to a decrease of the BF$_3$-THP signal (from 0.1 to 0.040 M) and an increase of the BF$_4^-$ signal (from 0.3 to 0.368 M), indicating the occurrence of the LiF dissolution and formation of LiBF$_4$ according to equation (2):

$$BF_3\text{-}THP\,(l) + LiF\,(s) \rightarrow LiBF_4\,(l) + THP\,(l) \tag{2}$$

The conversion of LiF into soluble LiBF$_4$ via BF$_3$-THP shows that BF$_3$-THP in the electrolyte solution can mediate inter-particle diffusion of LiF. As depicted in Fig. 8g, the LiF particles in the initially formed SEI exhibit a negative effective surface energy through LiBF$_4$ adsorption; this leads to a thermodynamic driving force towards fine structure with small LiF size. BF$_3$-THP initiates the dissolution of the initial large LiF, which results in LiBF$_4$ formation and BF$_3$-THP consumption in the SEI matrix, according to equation (2). By the out-of-equilibrium state, LiBF$_4$ regenerates BF$_3$-THP, while precipitating LiF with small LiF size, according to equation (1). The dissolution and re-precipitation of LiF, driven by the negative effective surface energy and mediated by BF$_3$-THP, eventually reduce the particle size of LiF and the inter-particle space.

We further examined the effect of the LiF restructuring on the electrical property and electrolyte swelling of the SEI. The bandgap of the SEI was nearly unchanged after restructuring (Supplementary Fig. 44 and Supplementary Note 4), whereas the swelling ratio of the SEI was notably reduced (Supplementary Figs. 45 and 46 and Supplementary Note 5). These results indicate that LiF restructuring inhibits the permeation of electrolyte molecules into the SEI owing to the reduced inter-particle space and thus suppresses Li corrosion.

Discussion

In addition to the presented borate–pyran electrolyte, the combination of a borate salt and other ether solvents also induce LiF dissolution/re-precipitation in an SEI as demonstrated in Supplementary Figs. 47–49 and Supplementary Note 6. This generality of the SEI restructuring mechanism indicates the possibility of adjusting the SEI restructuring ability by controlling the equilibrium constant for BF$_3$ association and dissociation based on various solvent molecules. Thus, a myriad of approaches for restructuring SEIs can be devised, for example, acceleration of SEI restructuring to minimize cumulative Li corrosion during the contact time between Li and liquid electrolyte. Finding new electrolyte

formulations that can lead to more efficient SEI restructuring while exhibiting high reduction stability (Fig. 3c,d and Supplementary Fig. 11) could advance LMB technology.

For the borate–pyran electrolyte, the irreversible Li loss is mainly attributed to dead Li; this result is in contrast to the previously reported high-CE electrolytes[3]. The high-CE electrolytes reported thus far exhibit a limiting Coulombic efficiency value of 99.6% (refs. 9,10,21), and further decreasing the Coulombic inefficiency is a considerable challenge owing to their high Li corrosiveness. However, the Coulombic efficiency of borate–pyran electrolyte is expected to be further improved using various methods that can suppress dead Li formation, such as pressure control, temperature control, current collector design and interfacial layer design, realizing Coulombic efficiencies beyond 99.85%.

Conclusions

In this study, we demonstrated that suppressing Li corrosion is an effective way to overcome the limitations of state-of-the-art electrolytes for Li-metal anodes. The cryo-TEM analysis results demonstrated that the restructured SEI minimized the direct contact between Li and the liquid electrolyte, thereby effectively mitigating Li corrosion. Together with a densely packed Li deposit morphology, the suppressed Li corrosion led to a high Li plating/stripping efficiency (average CE of 99.85%). Prototype Li||NCM811 pouch cells exhibited high cycling stabilities under lean electrolyte conditions, demonstrating the importance of limiting the Li corrosion in liquid electrolytes. The dissolution and re-precipitation of LiF mediated by the BF$_3$-THP paves a promising way to engineer SEI structure for advanced LMBs.

Methods

Electrolytes

Electrolyte preparation was performed in an argon-filled glovebox. One molar LiPF$_6$ EC:EMC (1:1 v/v, Phanax) + 2% VC (99.5%, Sigma-Aldrich) and 1.5 M LiFSI (99.9%, Sigma-Aldrich) in DME (99.5%, Sigma-Aldrich):TTE (97%, SynQuest Labs) (22:78, v/v) were used as control electrolytes. THP (anhydrous, 99%), LiBF$_4$ (99.99%) and LiTFSI (99.95%) were purchased from Sigma-Aldrich. FEC (98%) was purchased from TCI. A 0.4 M LiBF$_4$, 0.4 M LiTFSI THP + 20% FEC was used as borate–pyran electrolyte. A 0.8 M LiBF$_4$, 0.4 M LiTFSI THP + 20% FEC electrolyte was used for Li||NCM811 full cell tests.

Li morphology and SEI characterization

SEM images were obtained via a field-emission scanning electron microscope (Sirion, FEI). The cross-section images deposited Li (0.5 mA cm^{-2} and 2 mAh cm^{-2}) were obtained via a focused ion beam system (Helios Nanolab 450 F1, FEI); cross-section cleaning was performed at 5 kV and 0.3 nA to remove the damaged layer by Ga ions. The composition of the SEI layer on deposited Li was analysed by in situ XPS (Axis-Supra, Kratos) with an X-ray source (Al, $h\nu = 1,486.7$ eV). The sample inlet was directly connected to an argon-filled glovebox (<0.1 ppm of O$_2$ and H$_2$O) to prevent exposure of the sample to the atmosphere.

Cryo-TEM and image processing

To observe the fine structure of the SEI on Li while minimizing air reaction and beam damage, cryo-TEM analysis was carried out using a Glacios (Thermo Fisher) microscope with 200 kV accelerating voltage. A Li-deposited (1.0 mA cm^{-2} and 1.0 mAh cm^{-2}) TEM grid (200 mesh Cu with a lacey carbon film) was placed in a microtube (Eppendorf) inside an argon-filled glovebox, then removed and immediately placed in liquid nitrogen. The prepared sample grids were loaded into a cryo-autoloader (Glacios), ensuring that the samples were thoroughly cryogenic throughout the entire process, before being transferred into the cryo-TEM instrument. The obtained TEM images were converted to the FFT and inverse FFT images through the Gatan Microscopy Suite software. Inverse FFT images were obtained by applying bandpass masks (smooth edge: 5 pixels) to the crystal signals displayed in the

FFT and inverse-transforming them again. A black body colour table was applied to the inverse FFT images to visualize the crystallites. The SEI thickness and LiF size distribution were measured using the Image J programme.

Titration gas chromatography

Quantitative TGC analysis of Li loss due to dead Li and SEI Li$^+$ formation was carried out according to a previously reported procedure[3]. After applying the Aurbach method, the copper current collector and separator were placed in a 30 ml septa vial and tightly sealed at 1 atm. After that, the H$_2$ and Ar gas mixture obtained after injecting 1.0 ml of water into the vial was extracted through a syringe and injected into the TGC instrument (Agilent 7890A, Agilent Technology). Ar was used as carrier gas in the GC system. The H$_2$ concentration was calculated by comparing the hydrogen signals (0.545 retention time) in spectra obtained through a thermal conductivity detector with a calibration curve built using reference gases (250, 500 and 1,000 ppm H$_2$ in Ar).

NMR experiments

^{1}H and ^{19}F NMR measurements were performed using a 600 MHz liquid NMR spectrometer (Avance Neo 600, Prodigy probe). A BF$_3$-THP:THP solution was prepared by adding BF$_3$-THF as a BF$_3$ source in THP. Adding a small amount (0.1 M) of BF$_3$-THF into THP generated BF$_3$-THP and free THF (BF$_3$-THF + THP → BF$_3$-THP + THF). The BF$_3$-THP:THP solution was obtained via evaporation of THF (Boiling point = 66 °C) by heating at 70 °C. To collect the remaining electrolyte in the cycled pouch cells, they were injected with 1.5 ml of DMC solvent and gently shaken for 5 min. The extracted solution was then mixed with 400 µl of 0.1 M fluorobenzene in DMSO-d_6, and the final solution was analysed by NMR. The residual molar amounts were determined from the relative intensity of each component to the internal reference: DMSO-d_6 for EC, EMC, VC, DME and THP in the ^{1}H spectra and fluorobenzene for PF$_6^-$, FSI$^-$, TTE, BF$_4^-$, TFSI$^-$ and FEC in the ^{19}F spectra. The electrolyte consumption degree (ΔM, mol l^{-1}) was calculated from the difference between the residual molar amounts before and after cycling.

Pouch cell preparation

To prepare prototype pouch cells, two Li anodes (free-standing 40 µm or 20 µm, Honjo Metal), two Cu foils (MTI, rinsed with hydrochloric acid, acetone and deionized water in sequence) and double side-coated LiNi$_{0.8}$Mn$_{0.1}$Co$_{0.1}$O$_2$ (NCM811, provided by LG Energy Solution, 18.78 mg cm^{-2} loading, active material/Super P C65/Polyvinylidene fluoride = 96:2:2) were cut into 40 mm × 60 mm and 30 mm × 50 mm pieces, respectively. Ni and Al tabs were welded onto the Cu foil and NCM cathode, respectively, using an welding machine (WC-TW-300SJ, wellcos). The electrodes and the separator (19 µm polyethylene, W-Scope) were stacked and sealed with an aluminium pouch film and injected with 1.92, 1.24 or 0.96 g Ah^{-1} of electrolytes. The capacity of the bi-cell is 0.1 Ah at 1.0 C discharge. The cell preparation was performed in an argon-filled glovebox.

Energy density calculations

The areal mass of the bi-cell was calculated by adding the areal weights of a double-sided cathode (with Al current collector), two separator sheets, a double-sided anode (with Cu current collector) and a liquid electrolyte. The specific energy densities were calculated by dividing the areal energy of the bi-cell by the areal mass. The areal weights of the cell ingredients and cell design parameters, including the E/C ratio and average voltage, are provided in Supplementary Table 2.

Electrochemical analyses

Unless otherwise specified, electrochemical measurements were carried out using 2032-type coin cells with 50 µl of electrolyte. For the measurements of the average CE (pouch cell configuration, 40 mm × 60 mm Cu foil as a working electrode, 30 mm × 20 mm 150 µm

Li anode on 50 mm × 30 mm Cu foil as a counter electrode and polypropylene separator were used. A glass fibre separator was inserted in between the separator and counter electrode to prevent cell shorting by the edge burr of the Cu foil; we adopted the following standard protocol: (1) perform formation cycles with 5 mAh cm^{-2} of Li plating on Cu at 0.5 mA cm^{-2} and stripping to 1.0 V; (2) form initial Li source by plating 5 mAh cm^{-2} of Li on Cu at 0.5 mA cm^{-2}; (3) perform ten cycles at 1 mAh cm^{-2} and 0.5 mA cm^{-2}; (4) strip remaining Li from Cu to 1.0 V. Before the CE measurement, the Li||Cu cell was held at 0 V for 24 h, followed by cycling to form an SEI on the Cu current collector. EIS measurements (1470E frequency response analyser, Solartron Analytical) for ionic conductivity and interfacial resistance were conducted across a frequency range spanning from 1 MHz down to 0.1 Hz, using a perturbation amplitude of 10 mV. Li||NCM811 pouch cells were operated under pressurization at a clamping torque of 491 N cm, using a pressure jig and silicon pads (1 mm thickness). The applied initial pressure was 286 kPa. Galvanostatic cycling of the pouch cells was conducted within a voltage window of 4.25–3.0 V using a WBCS3000L battery tester at 25 °C, unless otherwise specified. The cells were first charged (0.1 C) and discharged (0.5 C) three times initially as a formation protocol, then performed 0.2 C charge/1.0 C discharge in subsequent cycles.

DFT and MD simulations

For DFT calculations, we adopted Materials Studio package with DMol^3 module. Perdew–Burke–Ernzerhof gradient-corrected exchange correlation functional was used. We used a double-numerical-plus-polarization version 4.4 function. A global orbital cut-off of 4 Å was applied. The COSMO or COSMO-RS were used to simulate the solvent environment (that is, solvation free energy). The COSMO method delivers the solvation free energy under a fixed solvent dielectric constant, $\varepsilon_{solvent}$, in a diluted environment. Conversely, the COSMO-RS simulates a concentrated environment because it calculates the solvation free energy for a solvation structure in its continuum. The energy (0.00001 Ha), gradient (0.002 Ha Å^{-1}) and displacement (0.005 Å) convergence criteria were set. The self-consistent-field cycles tolerance was 1.0×10^{-6} eV per atom. The reduction potential of the solvent molecules or Li$^+$ primary solvation sheath (E_{red}) was calculated using the thermodynamic energy cycles, which can be expressed by equation (3):

$$E_{red}\left(\text{V versus Li/Li}^+\right) = -\frac{(\Delta E_a + \Delta G_S(\text{sol}^-) - \Delta G_S(\text{sol}))}{F} - 1.4 \quad (3)$$

where ΔE_a is the electron attachment energy at 0 K; ΔG_S (sol$^-$) is the solvation free energy of reduced structure and ΔG_S (sol) is the solvation free energies of the initial structures (Supplementary Table 3); F is the Faraday constant (96,485 C mol^{-1}). To account for the difference between absolute electrochemical potential and Li/Li$^+$ scales, a correction factor of 1.4 is used. This correction factor may fluctuate within the range of 0.1–0.3 V considering the Li free energy in different electrolyte environments[50,51].

Molecular dynamics calculations were carried out using Materials Studio package with Forcite module. All components were filled in a periodic cell with optimized geometries and charges determined by DFT. We used the COMPASS III force field along with Ewald electrostatic and atom-based van der Waals as summation methods. Periodic cells constituted with 4 M LiFSI DME (40 Li$^+$, 40 FSI$^-$ and 56 DME) and 0.4 M LiBF$_4$, 0.4 M LiTFSI THP + 20% FEC (16 Li$^+$, 8 BF$_4^-$, 8 TFSI$^-$, 162 THP and 57 FEC) were simulated at 298 K and 1 atm. The cells were geometry optimized using Smart Algorithm with a convergence tolerance of 0.001 kcal mol^{-1} Å^{-1}. The cells were equilibrated by 1 ns in the NPT (fixed number, pressure and temperature) and NVT (fixed number, volume and temperature) using the Nosè algorithm with a Q ratio of 0.1. After equilibration, a 5-NVT with a time step of 1 fs was carried out with configurations saved every 5,000 fs.

Thermodynamic analysis

An investigation on the spontaneous size reduction process of LiF was conducted by calculating the chemical potential change of the size reduction reaction with fixed number of Li and F atoms, that is, conservative system. The chemical potential (eV per Li–F) of the LiF particles can be calculated by equation (4)[36]

$$\mu_{LiF}(d) = -\varepsilon_{LiF} + \frac{2a_{LiF}}{d_{LiF}} \Gamma_{LiF} \qquad (4)$$

where $\mu_{LiF}(d)$ is the chemical potential of LiF particles with diameter of d_{LiF}, ε_{LiF} is the cohesive energy per Li–F atoms (that is, E_{single} LiF in THP – E_{bulk} LiF), a_{LiF} is interatomic distance between Li and F atoms and Γ_{LiF} is the effective surface energy per surface Li–F atoms. Γ_{LiF} is the sum of the surface energy and adsorption energy considering the equilibrium of the surface reaction (that is, the reaction energy of $LiF + LiBF_4 \rightarrow LiF - Li^+ - BF_4^-$), which can be calculated as shown in equation (5)[36]

$$\Gamma_{LiF} = \gamma_{LiF} - kT \ln\left(1 + e^{-\Delta E/kT} n_{LiBF_4}\right) \qquad (5)$$

where γ_{LiF} is the surface energy per surface of Li–F atoms, k is the Boltzmann constant, T is the temperature, ΔE is adsorption energy and n_{LiBF_4} is number density of $LiBF_4$ in the electrolyte. Surface energy γ is a function of particle size. We calculated the surface energy of the infinite plane of LiF_{100} (most stable LiF facet, denoted as γ^∞) and the surface energy of spherical LiF cluster containing 16 of each Li and F atoms ($\gamma^{0.594nm}$) through DFT and obtained the fitting curve based on the rational expression[36]. γ^∞ and $\gamma^{0.594nm}$ were calculated using equation (6) based on DFT (γ^∞=0.103 eV per Li–F atoms, $\gamma^{0.594nm}$ = 0.415 eV per Li–F atom), and the fitting curve can be given as equation (7):

$$\gamma = \frac{E_{slab\ or\ particle} - NE_{bulk}}{S} \qquad (6)$$

$$\gamma_{LiF}(d) = \gamma^\infty + \frac{A}{(d_{LiF}/a_{LiF})} \qquad (7)$$

where $E_{slab\ or\ particle}$ is total energy of LiF slab or LiF particle, NE_{bulk} is total energy of N (N is number of Li and F atoms in slab or particle) number of Li and F atoms in bulk LiF crystal and S is number of Li–F pairs on the surface of slab or particle. A is a constant which can be obtained by inserting $\gamma^{0.594nm}$ = 0.415 eV per Li–F atoms. LiF precipitation occurs in the SEI matrix, but the DFT calculation was conducted using dielectric constant of THP considering the environment in which the SEI matrix was swollen by borate–pyran electrolyte. If the surface energy of LiF can be stabilized by interacting with SEI matrix, the size reduction of LiF particles will be more spontaneous.

MD simulations for chemical potential calculation were performed with infinite slab of LiF (1,000 Li–F pairs in unit cell), 256 Li–F cluster and 32 Li–F cluster with or without 100, 96, 32 of $LiBF_4$, respectively, in THP solvent molecules. The chemical potential of LiF particles based on MD was calculated using equation (8):

$$\mu_{LiF}(d) = \frac{E_{total} - N_{LiF}E_{LiF\ pair\ in\ THP} - N_{LiBF_4}E_{LiBF_4\ pair\ in\ THP} - N_{THP}E_{THP}}{N_{LiF}} \qquad (8)$$

where E_{total} is a total energy of the constructed cell containing LiF or LiF/$LiBF_4$ particle in THP, N_{LiF} is the number of Li–F pairs in the LiF particle, $E_{LiF\ pair\ in\ THP}$ is the energy of a single Li–F pair in THP, N_{LiBF_4} is the number of $LiBF_4$ adsorbed on LiF surface, $E_{LiBF_4\ pair\ in\ THP}$ is the energy of a single $LiBF_4$ pair in THP and $N_{THP}E_{THP}$ is the total energy of THP molecules in the constructed cell.

Data availability

The data supporting the findings of this study are included within the article and its Supplementary Information files. Source data are provided with this paper.

References

1. Liu, J. et al. Pathways for practical high-energy long-cycling lithium metal batteries. *Nat. Energy* **4**, 180–186 (2019).
2. Niu, C. et al. Balancing interfacial reactions to achieve long cycle life in high-energy lithium metal batteries. *Nat. Energy* **6**, 723–732 (2021).
3. Fang, C. et al. Quantifying inactive lithium in lithium metal batteries. *Nature* **572**, 511–515 (2019).
4. Niu, C. et al. High-energy lithium metal pouch cells with limited anode swelling and long stable cycles. *Nat. Energy* **4**, 551–559 (2019).
5. Qian, J. et al. High rate and stable cycling of lithium metal anode. *Nat. Commun.* **6**, 6362 (2015).
6. Jiao, S. et al. Stable cycling of high-voltage lithium metal batteries in ether electrolytes. *Nat. Energy* **3**, 739–746 (2018).
7. Ren, X. et al. Localized high-concentration sulfone electrolytes for high-efficiency lithium metal batteries. *Chem* **4**, 1877–1892 (2018).
8. Ren, X. et al. Enabling high-voltage lithium metal batteries under practical conditions. *Joule* **3**, 1662–1676 (2019).
9. Yu, Z. et al. Rational solvent molecule tuning for high-performance lithium metal battery electrolytes. *Nat. Energy* **7**, 94–106 (2022).
10. Yu, Z. et al. Molecular design for electrolyte solvents enabling energy-dense and long-cycling lithium metal batteries. *Nat. Energy* **5**, 526–533 (2020).
11. Zhang, J.-G., Xu, W., Xiao, J., Cao, X. & Liu, J. Lithium metal anodes with non-aqueous electrolytes. *Chem. Rev.* **120**, 13312–13348 (2020).
12. Cheng, X.-B. et al. A review of solid electrolyte interphases on lithium metal anode. *Adv. Sci.* **3**, 1500213 (2016).
13. Boyle, D. T. et al. Corrosion of lithium metal anodes during calendar ageing and its microscopic origins. *Nat. Energy* **6**, 487–494 (2021).
14. Weber, R. et al. Long cycle life and dendrite-free lithium morphology in anode-free lithium pouch cells enabled by a dual-salt liquid electrolyte. *Nat. Energy* **4**, 683–689 (2019).
15. Yan, C. et al. An armored mixed conductor interphase on a dendrite-free lithium metal anode. *Adv. Mater.* **30**, 1804461 (2018).
16. Liu, S. et al. In situ solid electrolyte interphase from spray quenching on molten Li: a new way to construct high-performance lithium metal anodes. *Adv. Mater.* **31**, 1806470 (2019).
17. Louli, A. J. et al. Diagnosing and correcting anode-free cell failure via electrolyte and morphological analysis. *Nat. Energy* **5**, 693–702 (2020).
18. He, X. et al. The passivity of lithium electrodes in liquid electrolytes for secondary batteries. *Nat. Rev. Mater.* **6**, 1036–1052 (2021).
19. Wang, A., Kadam, S., Li, H., Shi, S. & Qi, Y. Review on modeling of the anode solid–electrolyte interphase (SEI) for lithium-ion batteries. *npj Comput. Mater.* **4**, 15 (2018).
20. Li, Y. et al. Atomic structure of sensitive battery materials and interfaces revealed by cryo–electron microscopy. *Science* **358**, 506–510 (2017).
21. Cao, X. et al. Monolithic solid–electrolyte interphases formed in fluorinated orthoformate-based electrolytes minimize Li depletion and pulverization. *Nat. Energy* **4**, 796–805 (2019).
22. Ellis, L. D., Hill, I. G., Gering, K. L. & Dahn, J. R. Synergistic effect of $LiPF_6$ and $LiBF_4$ as electrolyte salts in lithium-ion cells. *J. Electrochem. Soc.* **164**, A2426–A2433 (2017).
23. Chang, Z. et al. Beyond the concentrated electrolyte: further depleting solvent molecules within a Li^+ solvation sheath to stabilize high-energy-density lithium metal batteries. *Energy Environ. Sci.* **13**, 4122–4131 (2020).

24. Yan, C. et al. Toward critical electrode/electrolyte interfaces in rechargeable batteries. *Adv. Funct. Mater.* **30**, 1909887 (2020).

25. Su, C.-C. et al. Solvating power series of electrolyte solvents for lithium batteries. *Energy Environ. Sci.* **12**, 1249–1254 (2019).

26. Chen, Y. et al. Steric effect tuned ion solvation enabling stable cycling of high-voltage lithium metal battery. *J. Am. Chem. Soc.* **143**, 18703–18713 (2021).

27. Adams, B. D., Zheng, J., Ren, X., Xu, W. & Zhang, J.-G. Accurate determination of Coulombic efficiency for lithium metal anodes and lithium metal batteries. *Adv. Energy Mater.* **8**, 1702097 (2018).

28. Tan Darren, H. S. et al. Carbon-free high-loading silicon anodes enabled by sulfide solid electrolytes. *Science* **373**, 1494–1499 (2021).

29. Attia, P. M., Chueh, W. C. & Harris, S. J. Revisiting the $t^{0.5}$ dependence of SEI growth. *J. Electrochem. Soc.* **167**, 090535 (2020).

30. Boyle, D. T. et al. Transient voltammetry with ultramicroelectrodes reveals the electron transfer kinetics of lithium metal anodes. *ACS Energy Lett.* **5**, 701–709 (2020).

31. Lu, W., Zhang, L., Qin, Y. & Jansen, A. Calendar and cycle life of lithium-ion batteries containing silicon monoxide anode. *J. Electrochem. Soc.* **165**, A2179–A2183 (2018).

32. Zhang, Y. et al. Silicon anodes with improved calendar life enabled by multivalent additives. *Adv. Energy Mater.* **11**, 2101820 (2021).

33. Keil, P. et al. Calendar aging of lithium-ion batteries. *J. Electrochem. Soc.* **163**, A1872–A1880 (2016).

34. Łodziana, Z., Topsøe, N.-Y. & Nørskov, J. K. A negative surface energy for alumina. *Nat. Mater.* **3**, 289–293 (2004).

35. Rosowski, K. A., Vidal-Henriquez, E., Zwicker, D., Style, R. W. & Dufresne, E. R. Elastic stresses reverse Ostwald ripening. *Soft Matter* **16**, 5892–5897 (2020).

36. Burlakov, V., Bootharaju, M., Besong, T., Bakr, O. & Goriely, A. Reversing Ostwald ripening. Preprint at https://arxiv.org/abs/1412.6280 (2014).

37. Lai, F. Effect of negative surface energy on nanocrystal morphology. *J. Phys. Conf. Ser.* **1759**, 012014 (2021).

38. Khan, M. A. S. & Ganguly, B. Can surface energy be a parameter to define morphological change of rock-salt crystals with additives? A first principles study. *CrystEngComm* **15**, 2631–2639 (2013).

39. Xie, T., Li, S., Wang, W., Peng, Q. & Li, Y. Nucleation and growth of BaF_xCl_{2-x} nanorods. *Chem. Eur. J.* **14**, 9730–9735 (2008).

40. Tasker, P. W. The surface energies, surface tensions and surface structure of the alkali halide crystals. *Phil. Mag. A* **39**, 119–136 (1979).

41. Liu, Z. et al. Interfacial study on solid–electrolyte interphase at Li metal anode: implication for Li dendrite growth. *J. Electrochem. Soc.* **163**, A592 (2016).

42. Zhang, S. et al. Tackling realistic Li^+ flux for high-energy lithium metal batteries. *Nat. Commun.* **13**, 5431 (2022).

43. Laubengayer, A. & Finlay, G. Donor–acceptor bonding. I. Etherates of boron trifluoride. *J. Am. Chem. Soc.* **65**, 884–889 (1943).

44. Greenwood, N. & Martin, R. Boron trifluoride co-ordination compounds. *Q. Rev. Chem. Soc.* **8**, 1–39 (1954).

45. Gal, J.-F., Maria, P.-C., Yáñez, M. & Mó, O. Enthalpies of adduct formation between boron trifluoride and selected organic bases in solution: toward an accurate theoretical entry to Lewis basicity. *Molecules* **26**, 6659 (2021).

46. Nie, M., Madec, L., Xia, J., Hall, D. S. & Dahn, J. R. Some Lewis acid–base adducts involving boron trifluoride as electrolyte additives for lithium-ion cells. *J. Power Sources* **328**, 433–442 (2016).

47. Zuo, X. et al. Lithium tetrafluoroborate as an electrolyte additive to improve the high-voltage performance of lithium-ion battery. *J. Electrochem. Soc.* **160**, A1199 (2013).

48. Zhang, S. S. A review on electrolyte additives for lithium-ion batteries. *J. Power Sources* **162**, 1379–1394 (2006).

49. Friedrich, H. & Simon, J. Method for producing highly pure $LiBF_4$. US patent 6,537,512B1 (2003).

50. Chen, J. et al. Electrolyte design for LiF-rich solid–electrolyte interfaces to enable high-performance microsized alloy anodes for batteries. *Nat. Energy* **5**, 386–397 (2020).

51. Hayamizu, K., Aihara, Y., Arai, S. & Martinez, C. G. Pulse-gradient spin-echo ^1H, ^7Li, and ^{19}F NMR diffusion and ionic conductivity measurements of 14 organic electrolytes containing $LiN(SO_2CF_3)_2$. *J. Phys. Chem. B* **103**, 519–524 (1999).

Author contributions
H. Kwon and H.-T.K. conceived the idea and directed the project. H. Kwon designed the series of experiments involved in the study, including DFT/MD simulations, cryo-TEM/FIB-SEM analyses, electrochemical measurements, battery tests, TGC and NMR experiments. H. Kwon, W.O. and Y.R. contributed to the battery tests for optimizing the cycle performance. H. Kwon and J.H. contributed to analyse the TGC data. H. Kim and D.S. contributed to the battery design. All authors discussed and analysed the data. H. Kwon and H.-T.K. co-wrote and revised the paper, and H.-T.K. supervised the work.

Competing interests
H.-T.K., H. Kwon and H. Kim declare that this work has been filed for a KR Provisional Patent Application (number 10-2022-0105317). The other authors declare no competing interests.

Additional information
Supplementary information The online version contains supplementary material available at https://doi.org/10.1038/s41560-023-01405-6.

Correspondence and requests for materials should be addressed to Hee-Tak Kim.

Peer review information *Nature Energy* thanks the anonymous reviewers for their contribution to the peer review of this work.

Reprints and permissions information is available at www.nature.com/reprints.

Publisher's note Springer Nature remains neutral with regard to jurisdictional claims in published maps and institutional affiliations.